Journal of Terramechanics 120 (2025) 101058

Contents lists available at ScienceDirect

Journal of Terramechanics

journal homepage: www.elsevier.com/locate/jterra

Extending granular resistive force theory to cohesive powder-scale media

Deniz Kerimoglu [a,*], Eloïse Marteau [b], Daniel Soto [a], Daniel I. Goldman [a]

[a] School of Physics, Georgia Institute of Technology, 837 State St., Atlanta, 30318, GA, USA
[b] Jet Propulsion Laboratory, California Institute of Technology, 4800 Oak Grove Drive, Pasadena, 91109, CA, USA

ARTICLE INFO

Keywords:
Granular resistive force theory
Dry powder
Cohesion
Planetary lander footpad

ABSTRACT

Intrusions into granular media are common in natural and engineered settings (e.g. during animal locomotion and planetary landings). While intrusion of complex shapes in dry non-cohesive granular materials is well studied, less is known about intrusion in cohesive powders. Granular resistive force theory (RFT) — a reduced-order frictional fluid model — quantitatively predicts intrusion forces in dry, non-cohesive granular media by assuming a linear superposition of angularly dependent elemental stresses acting on arbitrarily shaped intruders. Here we extend RFT's applicability to cohesive dry powders, enabling quantitative modeling of forces on complex shapes during intrusion. To do so, we first conduct intrusion experiments into dry cornstarch powder to create stress functions. These stresses are similar to non-cohesive media; however, we observe relatively higher resistance to horizontal intrusions in cohesive powder compared to non-cohesive media. We use the model to identify geometries that enhance resistance to intrusion in cohesive powder, aiming to minimize sinkage. Our calculations, supported by experimental verification, suggest that a flat surface generates the largest stress across various intrusion angles while a curved surface exhibits the largest resistive force to vertical intrusion. Our model can thus facilitate optimizing design and movement strategies for robotic platforms (e.g. extraterrestrial landers) operating in such environments.

1. Introduction

1.1. Resistive force theory

Interactions of solid objects with granular media occur in a wide range of contexts, from engineered settings to natural interactions. Granular media exhibit complex behaviors when interacting with a rigid body, driven by friction-dominated inter-particle forces. Such interactions produce complex flow and force responses, with the material displaying both solid-like and fluid-like properties. The principles governing the interaction of rigid objects moving within plastically deforming media have been applied in robotics to develop machines (Bhushan, 2009; Maladen et al., 2009; Karsai et al., 2022) and vehicles (Bekker, 1960) capable of traversing granular surfaces. These complex interactions are fundamentally influenced by how local granular material properties generate global resistive forces on intruding objects.

To predict the role of granular terrain under rigid intrusions, one approach is to simplify the behavior of granular media into tractable force models. Granular resistive force theory (RFT), a reduced order frictional fluid model, has been proposed to provide quantitative predictions of quasi-static intrusion forces in dry, non-cohesive granular materials (Li et al., 2013; Maladen et al., 2011). Despite the complex properties of granular materials, RFT stands out for its remarkable simplicity and effectiveness (Schofield and Wroth, 1968; Kamrin, 2010; Kamrin and Koval, 2012; Henann and Kamrin, 2013). RFT has been successfully applied to understand and improve the granular locomotion of wheeled systems (Agarwal et al., 2021) and legged robots (Lee et al., 2020; Chong et al., 2021; Treers et al., 2022).

RFT operates by linear superposition of the elemental forces obtained by discretizing the surface of the arbitrarily shaped intruders. The total resistive force is approximated as the sum of the resistive forces acting on each discretized body element as if each element were independently moving. The physics underlying the success of granular RFT in predicting granular resistive forces has been numerically investigated in Askari and Kamrin (2016) through a frictional plasticity continuum partial differential eqaution model. The continuum model quantitatively matched experimental intrusion data and RFT predictions using two key mechanical properties of dry granular media: a frictional yield criterion and the absence of cohesion between particles. Despite its success, RFT has only been applied to predict intrusion behaviors in non-cohesive materials. The generality and applicability of the continuum model have yet to be verified for dry cohesive substrates.

Dry cohesive, fine particulate media (particle diameter smaller than 30 μm) is common in natural and artificial environments.

* Corresponding author.
E-mail address: dkerimoglu6@gatech.edu (D. Kerimoglu).

https://doi.org/10.1016/j.jterra.2025.101058
Received 7 December 2024; Accepted 13 April 2025
Available online 20 May 2025

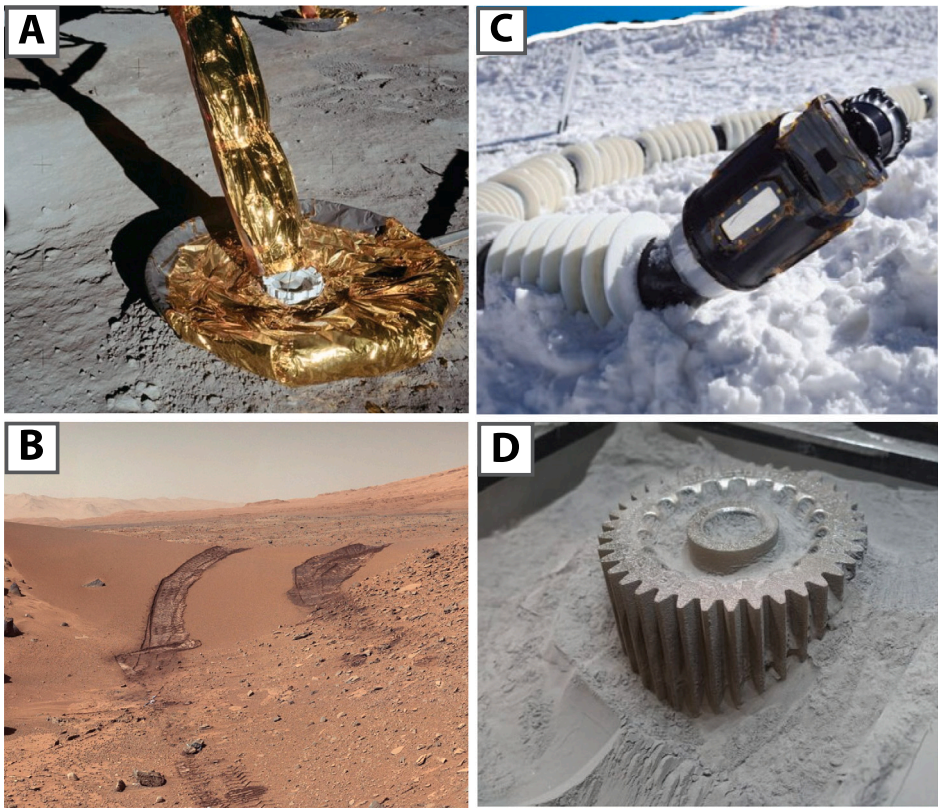

Fig. 1. Examples of dry cohesive powder-scale media A) Planetary lander footpad on the moon surface, (B) Mars regolith (C) EELS snake robot on loose snow, and (D) Metal powder 3D printing. Photo credits: (A) Apollo 11, Lunar Module Footpad (B) https://photojournal.jpl.nasa.gov/catalog/PIA17944 C) (Vaquero et al., 2024) D) https://www.heraeus-group.com/en/.

Examples include extraterrestrial settings with legged (Fig. 1A) and wheeled (Fig. 1B) systems on regolith, robotic systems navigating loosely consolidated snow (Fig. 1C), and metal powder in 3D printing processes (Fig. 1D). The cohesion observed between dry powder particles arises primarily from Van der Waals forces or electrostatic interactions (Castellanos, 2005; Feng and Hays, 2003). However, cohesive media resistive forces can still be generated locally based on the rigid body's shape during intrusion. In other words, as predicted by Askari and Kamrin (2016), when moving through cohesive powder the elemental forces on an intruder's segments are expected to depend only on its position, orientation, and direction of motion, without cross-correlation between body segments. We hypothesize that the linear superposition principle of non-cohesive granular RFT can be extended to cohesive powders.

1.2. Planetary lander footpads

In the solar system, various fine regolith materials are known to exhibit cohesive properties. Geotechnical measurements and sample analyses from the Apollo missions have demonstrated that the lunar regolith exhibits considerable cohesion, particularly within its finer particles (Heiken et al., 1991; Slyuta, 2014). On Mars, observations of trenches and scrapes created by lander scoops, footpad imprints, and rover tracks have revealed that Martian regolith exhibits cohesive properties (Moore and Jakosky, 1989; Moore et al., 1987; Team, 1997; Shaw et al., 2009; Arvidson et al., 2014; Golombek et al., 2020; Marteau et al., 2023). In the outer solar system, Enceladus and potentially Europa eject materials from their subsurface oceans into their exospheres, with some of this material settling back onto the surfaces of these Ocean Worlds. Plume deposits are expected to consist of fine-grained ice particles that evolve via sintering, possibly transforming initially unconsolidated deposits into consolidated porous ice (Choukroun et al., 2020; Molaro et al., 2019; Dhaouadi et al., 2022). Future exploration of these icy moons by a lander (MacKenzie et al., 2021; Hand et al., 2022) will require understanding the interactions between their surface material and landing footpads during a touchdown event. This is particularly relevant to the South Pole of Enceladus, which is of great scientific interest, where freshly deposited plumes are loosely consolidated, making successful landings challenging. Few studies have been conducted to understand the material properties (Jabaud et al., 2024) and the interaction of landing gear with such weak and cohesive surfaces (Harmon et al., 2023). As robotic space exploration advances, the cohesive properties of these various regolith types have significant implications for mission formulation, influencing mobility, instrumentation, and the design of landing systems across diverse planetary surfaces.

Terramechanics models used in planetary exploration have predominantly operated under the assumption that regolith is cohesionless, neglecting the cohesive properties present in extraterrestrial soils. Similarly, analyses of landing footpads have relied on outdated and conservative assumptions, primarily rooted in testing conducted during the Apollo era in the 1960s (Winters, 1968). Since then, there have been no comprehensive testing campaigns to evaluate landing footpad interactions with cohesive or complex regolith, highlighting a significant gap in our current understanding and design approaches for future planetary landers.

In this paper, we conduct systematic RFT experiments in dry cohesive powder, measuring intrusion forces to demonstrate that these forces can be linearly superimposed. We observe an approximately linear stress–depth relationship which we use to create stress per unit depth functions. We compare the stress profiles of cohesive and non-cohesive media and experimentally validate our powder RFT (PRFT) model. We observe that while the stress patterns in the cohesive powder are similar to those in non-cohesive granular media, the cohesive powder displays significantly higher resistance to horizontal intrusions. To

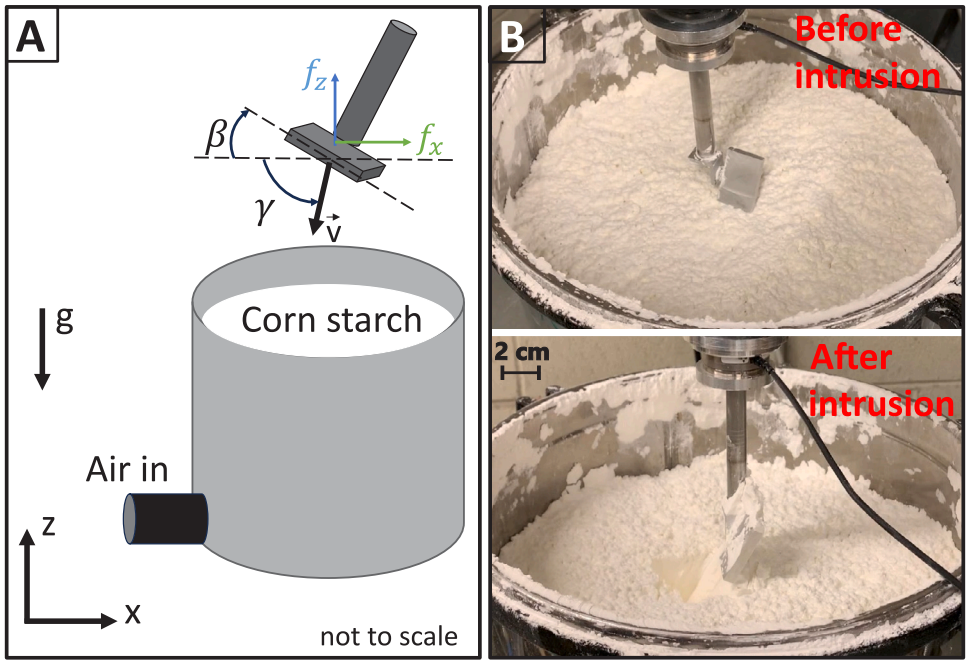

Fig. 2. Apparatus for controlled intrusion experiments into dry powder. A) Diagram of the test platform used for powder intrusion experiments. The chamber, filled with cornstarch powder, is connected to an air blower that facilitates the creation of a loosely consolidated powder state. A robot arm, along with the support rod holding the plate element, controlled the plate's attack and intrusion angles. B) An image of the cornstarch-filled chamber before and after the intrusion of the rod attached to the aluminum plate. Notice the crater formed after the intrusion. The substrate around the intrusion site did not substantially reconfigure, retaining its post-intrusion configuration due to inter-particle cohesion even after the intruder was removed.

utilize the predictive capabilities of our model, we identify geometries that enhance intrusion resistance in weak and cohesive surfaces, aiming to identify shapes for potential planetary lander footpads. We aim to minimize vertical sinkage during a landing event, posing landing stability challenges. We first create various model footpad shapes and conduct extensive PRFT calculations with them. We discover that a flat geometry, reflecting a disk-shaped footpad, generates larger stresses (force per unit area) than curved ones across a wide range of intrusion scenarios. Conversely, a curved geometry, due to increased surface area, generates more resistive force than a flat one, particularly under more vertical intrusion conditions. We validate our model's capabilities by experimentally testing diverse footpad geometries, observing a strong correlation between the experimental results and PRFT predictions.

2. Materials and methods

We developed an apparatus to perform systematic intrusion experiments Fig. 2A) into loosely consolidated dry powder. A stainless steel pressure chamber (30 cm in diameter and 40 cm in height) as shown in Fig. 2B is attached to an air blower. The chamber's interior features a honeycomb structure and a porous plastic layer, which facilitates the creation of a uniform airflow when the air blower is activated. We used cornstarch powder (particle diameter range 5 μm– 25 μm) as a model dry and cohesive powder substrate and filled the chamber to a depth of 17 cm. Before each experiment, we carefully applied air fluidization and mechanical agitation to set the powder to a loosely packed state (Skonieczny et al., 2019). We measured the bulk volume fraction $\phi = 0.35$ of the substrate by calculating the ratio of solid volume to occupied volume using the density of cornstarch particles (1.34 g/mL) (Fuentes et al., 2019).

The intrusion experiments are conducted using a robot arm (Denso Robotics) moving at a constant speed, $v = 1$ cm/s. We mounted a 6-axis force/torque sensor (ATI Industries Mini-40, SI-80) to the robot arm's end effector to capture powder resistive forces. A supporting rod with a connector is mounted on the force sensor, facilitating the attachment of an aluminum plate to the rod. The robot arm motion and the support rod connection enabled us to adjust the angle of intrusion γ and angle of attack β of the plate (dimensions 2.5 cm × 3.8 cm × 0.6 cm) as depicted in Fig. 2A). We measured the forces in the horizontal (x) and vertical (z) axes at 1 kHz during plate intrusion experiments. We first measured the forces on the supporting rod as it moved through the powder without the plate attached for each γ and β combination. Next, we repeated the intrusion with the rod and plate, subtracted the rod-only forces, and divided the result by the plate's surface area to calculate the stresses applied only on the plate. We used the stresses in the region away from the surface and the bottom of the chamber. We performed three experiments for each combination of γ and β and used their means to obtain stresses $\sigma_{z,x}$ for $-\pi/2 < \beta < \pi/2$ and $0 < \gamma < \pi/2$. The positive range for γ is selected because we are focused on the intrusion of objects. The stresses $\sigma_{z,x}$ for horizontal movements ($\gamma = 0$) were determined similar to Li et al. (2013), by fitting the stresses to the average values in the steady-state regions at depths of $z = 3$ cm, 6 cm, and 9 cm.

3. Results

3.1. Developing powder resistive force theory

Forces in horizontal and vertical axes are shown in Fig. 3A. We observed that for all β and γ tested the forces were nearly proportional to depth $|z|$, similar to lithostatic pressure observed in non-cohesive granular media (Li et al., 2013). Using this region of depth gave us linear relations between depth and stress, dashed orange fits in Fig. 3B and Fig. 3C.

These slopes are used to estimate the stiffness (stress per unit depth) of the substrate to the intruding plate, $\alpha_{z,x}$. The plate's angle of intrusion γ and attack β are varied to obtain the vertical and horizontal stress per unit depth relations as illustrated in Fig. 4. Stresses in the powder, in both directions, were sensitive to both the angles of attack

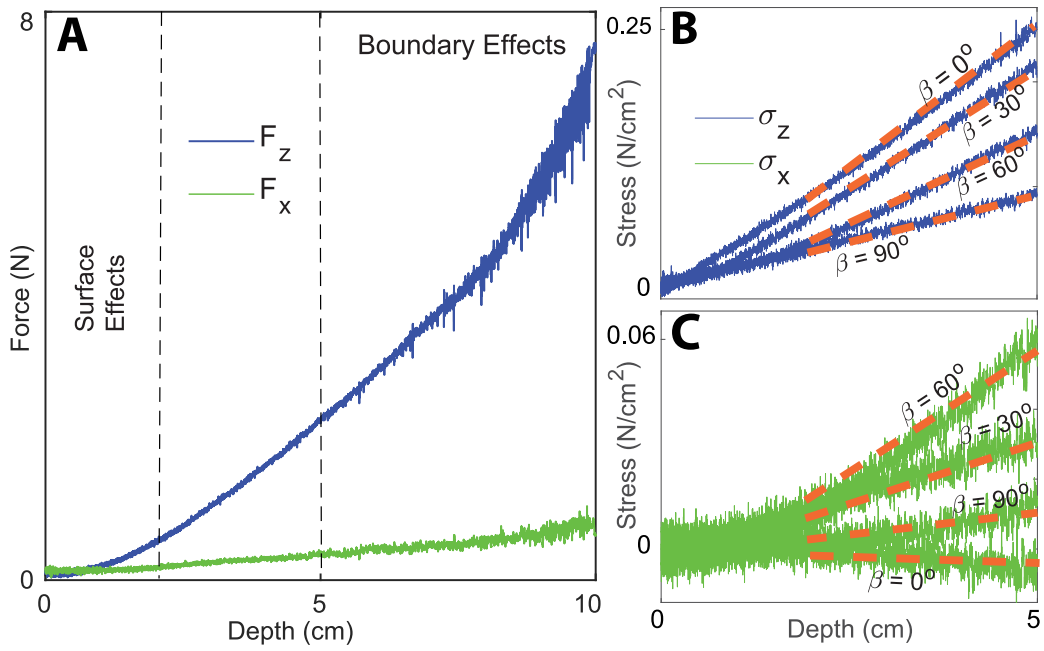

Fig. 3. Force and stress plots during intrusions at various angles of attack. (A) Force curves for z and x axes for $\gamma = 90°$ and $\beta = 30°$. (B) Stress curves (green and blue) for $\gamma = 90°$ and $\beta = [0°, 30°, 60°, 90°]$ and linear fits (dashed orange) to these curves. (For interpretation of the references to color in this figure legend, the reader is referred to the web version of this article.)

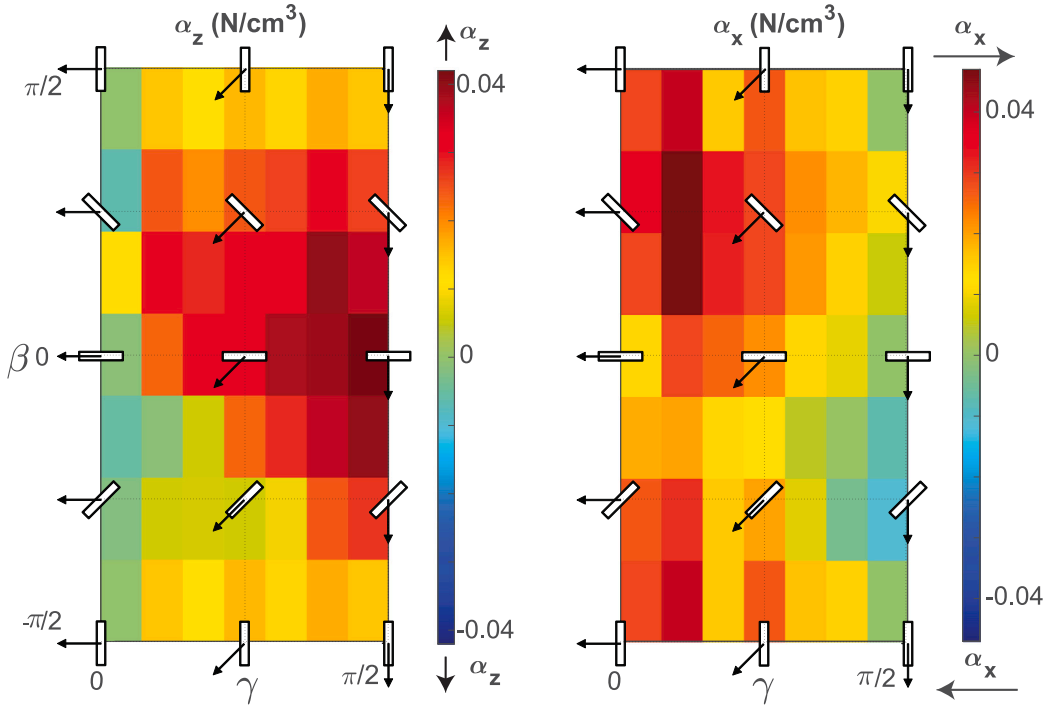

Fig. 4. Stress-per-unit-depth, $\alpha_{z,x}$, relations for vertical and horizontal directions. The individual grids correspond to the slopes of the fitted lines for $0 < \gamma < \pi/2$ and $-\pi/2 < \beta < \pi/2$.

and intrusion, showing qualitative similarities to those observed in the non-cohesive granular heatmap. In general, the media resisted the plate's motion across most values of β and γ, as indicated by positive stress values in the $\sigma_{z,x}$ plots. However, for certain combinations of β and γ, the material did not resist intrusion, which is reflected by negative values in the heatmap. For all γ (except for $\gamma = \pi/2$), $\alpha_{z,x}$ were asymmetric to angle of attack values $\beta = 0$ and $\beta = \pi/2$.

To interpolate intermediate stress values and compare cohesive and non-cohesive stress profiles we conducted a fitting approximation on powder stress per unit depth functions $\alpha_{z,x}$. Using the discrete Fourier Transform we obtained a fitting function in the form shown below, based on a similar approach in Li et al. (2013). The functions can be approximated as:

$$\alpha_z^{fit}(\beta,\gamma) = \sum_{m=-1}^{1}\sum_{n=0}^{1}[A_{m,n}cos2\pi(\frac{m\beta}{\pi}+\frac{n\gamma}{2\pi}) + B_{m,n}sin2\pi(\frac{m\beta}{\pi}+\frac{n\gamma}{2\pi})] \quad (1)$$

$$\alpha_x^{fit}(\beta,\gamma) = \sum_{m=-1}^{1}\sum_{n=0}^{1}[C_{m,n}cos2\pi(\frac{m\beta}{\pi}+\frac{n\gamma}{2\pi}) + D_{m,n}sin2\pi(\frac{m\beta}{\pi}+\frac{n\gamma}{2\pi})] \quad (2)$$

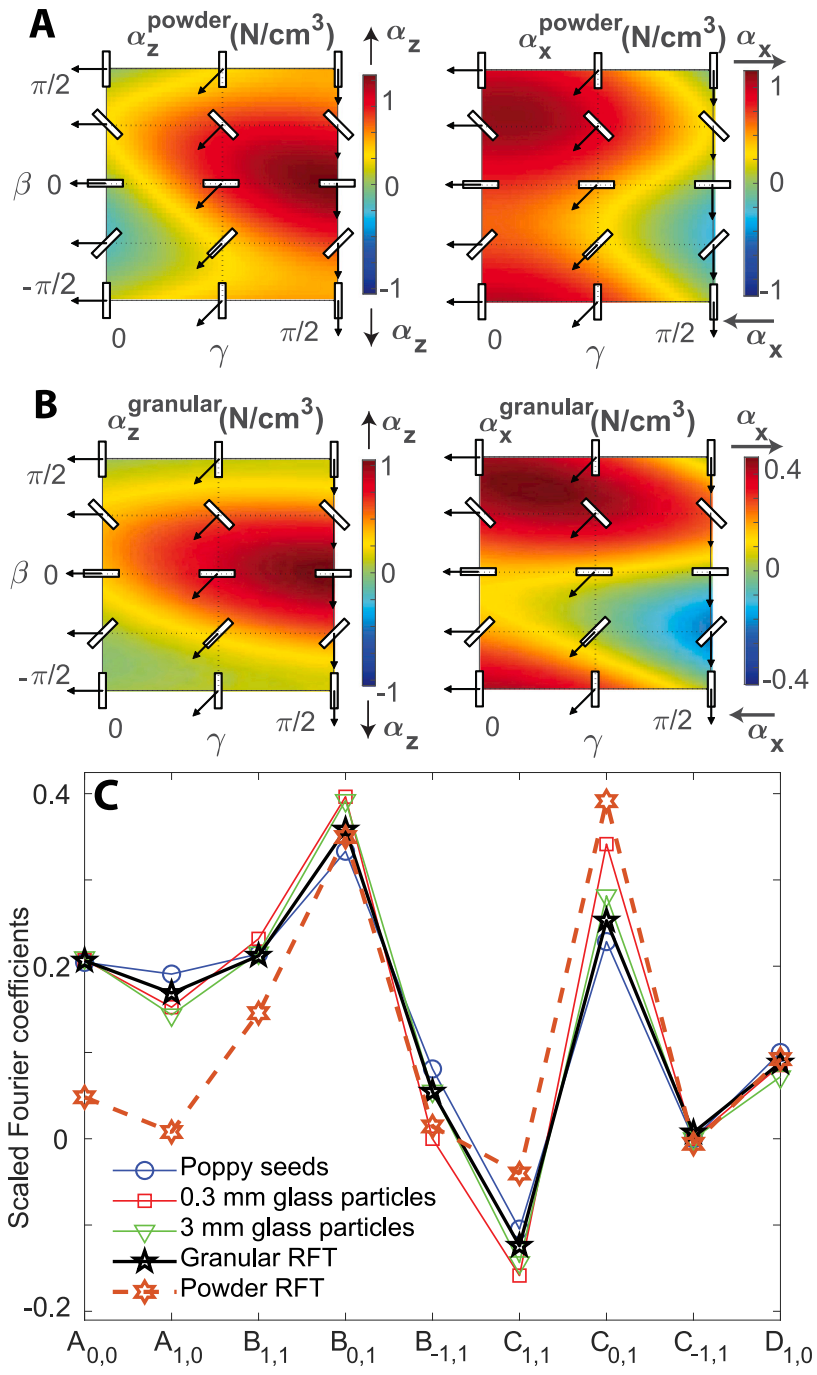

Fig. 5. Plots of stress per unit depth heatmaps obtained by the fitting functions for A) powder RFT (cohesive) and (B) granular RFT (non-cohesive). (C) Scaled Fourier coefficients of various non-cohesive and cohesive media.

The powder stress profiles using the fitting function are plotted in Fig. 5A, which we refer to as powder RFT (PRFT). We then adopted the granular stress per unit depth profiles from Li et al. (2013), as shown in Fig. 5B, representing granular media with particle sizes ranging from 0.3 mm to 3 mm for comparison purposes. Although qualitatively similar along both axes z and x-axes, we observed notable differences between the powder and granular heatmaps. Specifically, the material's resistance to penetration in the horizontal axis is significantly higher in the powder compared to the non-cohesive media. Additionally, the powder stresses exhibit larger resistance near $\beta = \pm\pi/2$ (the top and bottom regions of the heatmaps), unlike non-cohesive media, where resistance diminishes rapidly. In this dry powder regime, we attribute these differences to the cohesive nature of the material, which enables stronger inter-particle attractive forces than non-cohesive granular media. The lack of attractive forces between particles leads to more rapid stress diminution.

We then compared the scaled Fourier coefficients of the fitting functions in Eqs. (1) and (2) for powder and granular RFT, along with various non-cohesive granular materials. Fig. 5C shows the zeroth and first-order coefficients of these fitting functions. We observed that the coefficients for the powder exhibited similar trends to those of different non-cohesive granular materials.

3.2. Experimental validation of PRFT

As a next step, we tested if the forces acting on a more geometrically complex intruder moving in powder could be estimated by applying

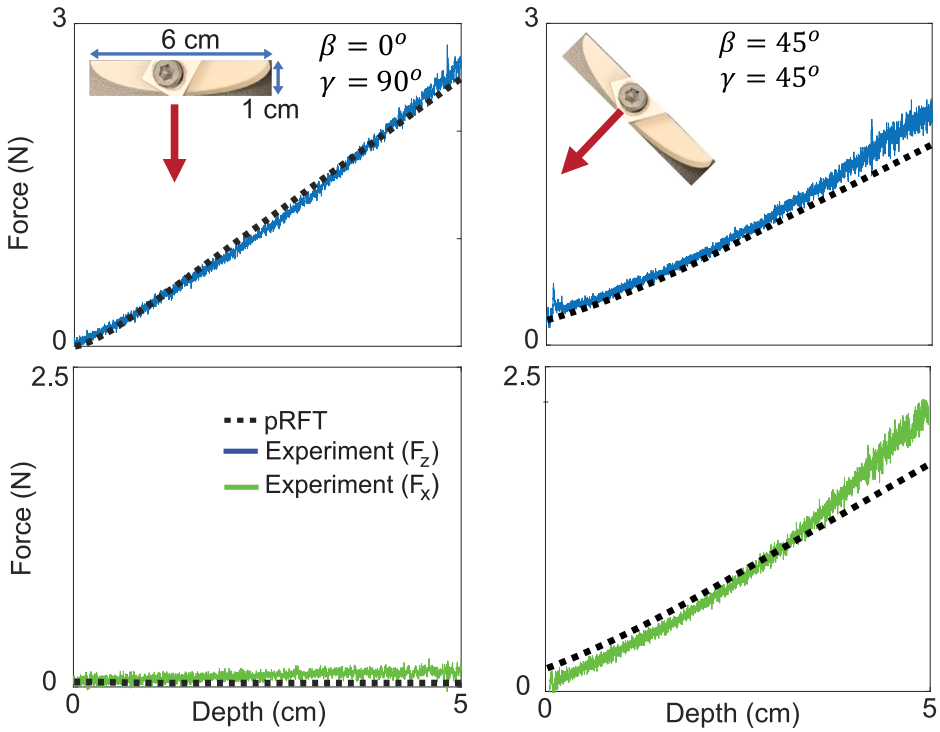

Fig. 6. Force curves obtained from powder intrusion experiments and powder RFT calculations for a curve-shape object. A comparison between the solid (experimental) and dashed (PRFT) lines show that our model largely predicts the total forces acting on the body through linear superposition.

linear superposition to the forces acting on small elements of the intruder. To this end, we conducted powder intrusion experiments with a curved geometry and measured its vertical (F_z) and horizontal (F_x) forces for two different β and γ scenarios (see Fig. 6). We then performed powder RFT calculations by discretizing the geometry into 30 small plate elements and integrating the stresses along the curve's leading edge (Askari and Kamrin, 2016). By plotting the measured (solid) and predicted (dashed) data in Fig. 6, we demonstrated that the PRFT calculations closely matched both the horizontal and vertical forces for both intrusion configurations.

3.3. Utilize PRFT to investigate lander footpad geometries

In this section, we showcase the predictive abilities of our model by using it to discover geometries that enhanced resistance to intrusion into loosely consolidated cohesive powder. This is particularly relevant for the design of extraterrestrial landing gear, where landing on extremely weak surfaces poses a significant challenge to mission success. Specifically, Enceladus' loosely consolidated and cohesive surface consisting of ice plume deposits is a prime example of such a terrain. Here, we are interested in how various geometries generate different reaction forces through extensive PRFT calculations. In doing so, we aim to identify geometries that enable reduced sinkage during intrusion into weak surfaces.

We started by creating footpad shapes by first meshing a 2D plane. The meshed region is 6 cm long (footpad length) and 3 cm deep (footpad depth) with grid sizes of 1 cm and 0.25 cm, respectively. Then, we fit splines along the intersections of these meshes giving us arbitrary shapes. Fig. 7A illustrates three sample footpad shapes.

Since our model only generates reaction forces as outputs, we intruded the geometries to a fixed depth to ensure a fair comparison among them. Starting from the surface, we intruded shapes to a depth of 5 cm for $\beta = 0°$ and $\gamma = 70°$ as illustrated in Fig. 7B. Fig. 7C illustrates the vertical (solid) and horizontal (dashed) force curves for three shapes, with the corresponding colors indicated in Fig. 7A. The vertical forces were larger than the horizontal forces since all shapes move primarily in a vertical direction within the media. Although the red and green footpads have different shapes, they exhibited similar force trends, particularly in the vertical direction. The blue shape, having a minimal contact surface area among others, produced the largest vertical force and the smallest horizontal force. The large vertical forces observed in the blue shape can be attributed to its greater horizontal segments, generating increased resistance to vertical movement, as shown with the red regions in Fig. 4. In contrast, the sharp and the wavy segments in other shapes resulted in reduced vertical resistance. The reduced horizontal resistance of the blue footpad can be attributed to its narrow thickness, whereas the other shapes are thicker and have a larger resistance to horizontal motion.

Next, we examined the resistive forces of all the arbitrary footpads we generated. Specifically, we calculated the vertical resistive forces at a given depth, as we focused on identifying shapes that generated maximal vertical forces. We conjecture that the greater the vertical resistive force a shape produces at a certain depth, the less sinkage the landing module will experience on a weakly consolidated surface. Thus, a shape that produces larger forces would result in less sinkage. We also explored shapes that produce minimal vertical force to gain a deeper understanding of the mechanisms behind force generation in the maximal-force shapes.

To ensure a fair comparison among the footpads, we made several assumptions about their intrusion. First, we assumed that the footpads make contact on a level surface, with the footpad's attack angle β parallel to the surface. We then assumed that the footpad's orientation remained constant during intrusion. In other words, the PRFT calculations assumed $\beta = 0$ during the intrusion, as we cannot predict how much deflection the leg will experience during the actual planetary landing. Additionally, since the angle of intrusion during a landing event is uncertain, we performed PRFT calculations for three γ scenarios: perfect vertical intrusion ($\gamma = 90°$), diagonal intrusion ($\gamma = 45°$), and near horizontal intrusion ($\gamma = 20°$). Consequently, the forces generated by the small-scale footpad can reasonably scale to those produced by a larger footpad during ground contact in a landing event, due to the principle of linear superposition. Therefore, our investigation

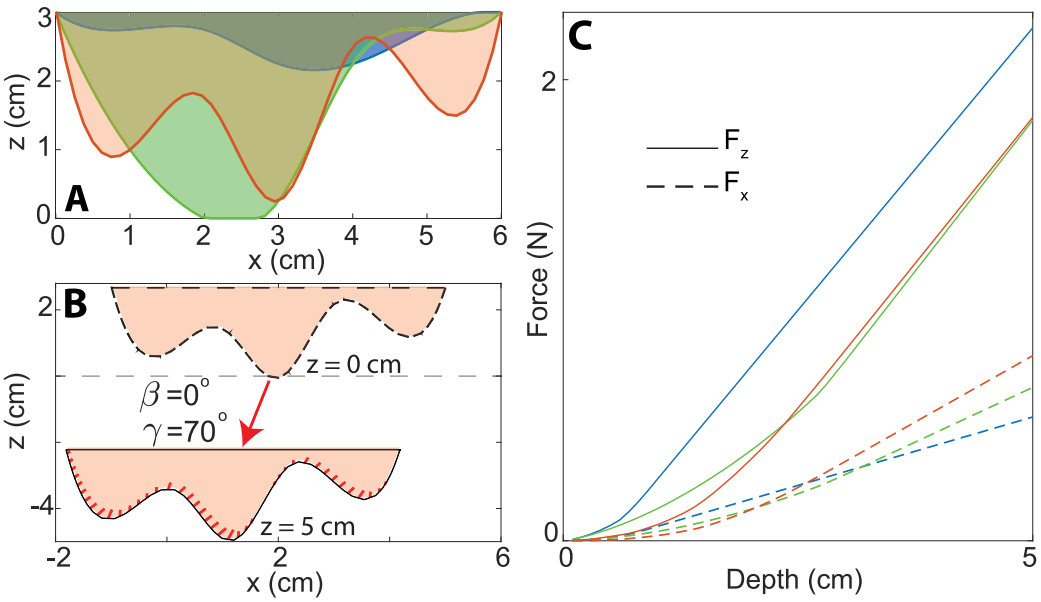

Fig. 7. Illustrations and force profiles of footpad geometries. (A) Sample footpad shapes illustrated as different colors generated via spline. (B) Illustration of a sample intrusion to a depth of 5 cm for $\beta = 0°$ and $\gamma = 70°$. (C) Forces of the footpad intrusion shown in Fig. 7B for z (solid) and x-axes (dashed) using PRFT.

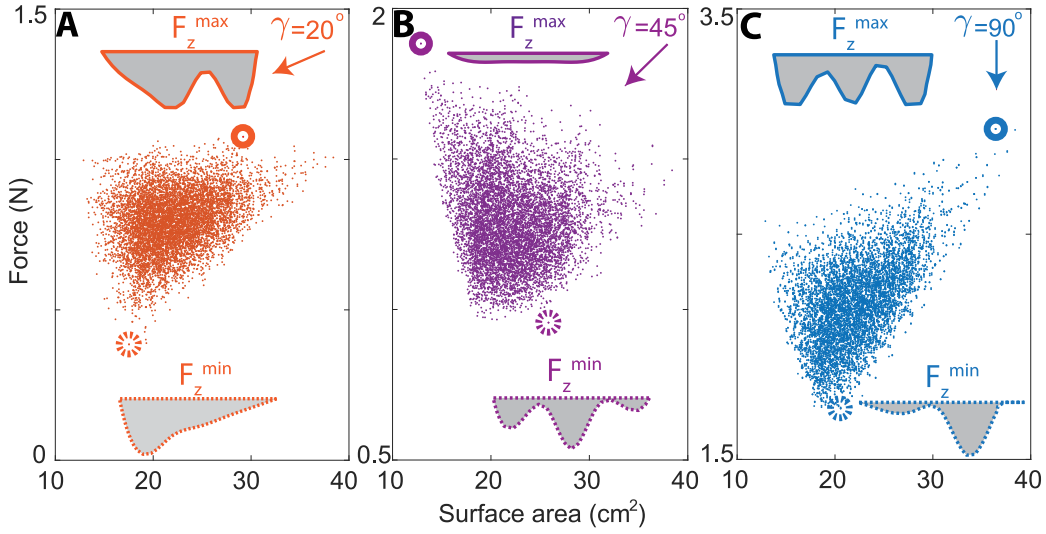

Fig. 8. PRFT peak force distributions of footpad geometries at an intrusion depth of 5 cm for three different angles of attack, illustrating the high variability in forces. Each point in Fig. 8A–C, represents the vertical force of individual footpad geometries (a total of 7776) as a function of their respective surface areas at a depth of 5 cm for $\gamma = [20°, 45°, 90°]$, shown from left to right, respectively.

will provide valuable insights into the design of large-scale footpads for NASA JPL's lander missions.

Our PRFT calculations revealed that the range of vertical forces varied significantly, depending on both the footpad geometry and the angle of intrusion. This variation is more pronounced for near-horizontal intrusion (orange) than other intrusion scenarios (purple for diagonal and blue for perfect vertical intrusion). We highlighted the shapes that generate the maximal and minimal vertical forces by encircling their respective points via dashed and solid circles and visualized them at the top and bottom of Fig. 8A–C. Examining the shapes that exhibit minimum forces across all intrusion scenarios revealed a common feature: they all have a large, sharp wedge-like form (shapes with dashed borders). The small vertical forces of wedge shapes can be attributed to their edges having larger angles of attack, which are associated with smaller stresses (yellow and green regions in Fig. 4). Additionally, in the near-horizontal intrusion scenario, the large wedge shape creates a shadowing effect (Suzuki et al., 2019), where forces are diminished in areas that lie in the immediate vicinity of another part of the intruder. In other words, the leading edge of the intruder (leftmost wedge), impedes the forces acting on the non-leading edge, which is the right part of the intruder.

In contrast, the shapes generating maximal forces did not share a common form (shapes with solid borders). However, curvy patterns that increase the contact surface area with the material tend to generate more force for $\gamma = 20°$ and $\gamma = 90°$. The increased surface area of the curvy footpad (solid blue and orange borders) likely contributes to this increase in force. Conversely, a flat surface with minimal surface area produced the largest vertical force in the diagonal intrusion and substantial forces in other intrusion scenarios (the leftmost point in all subfigures). This may be because most of the individual elements of flat shape penetrate to greater depths, generating more resistive force than more curvy shapes, whose curved edges penetrate the material gradually. Additionally, the curvy regions contribute to the shadowing effect, reducing the vertical forces.

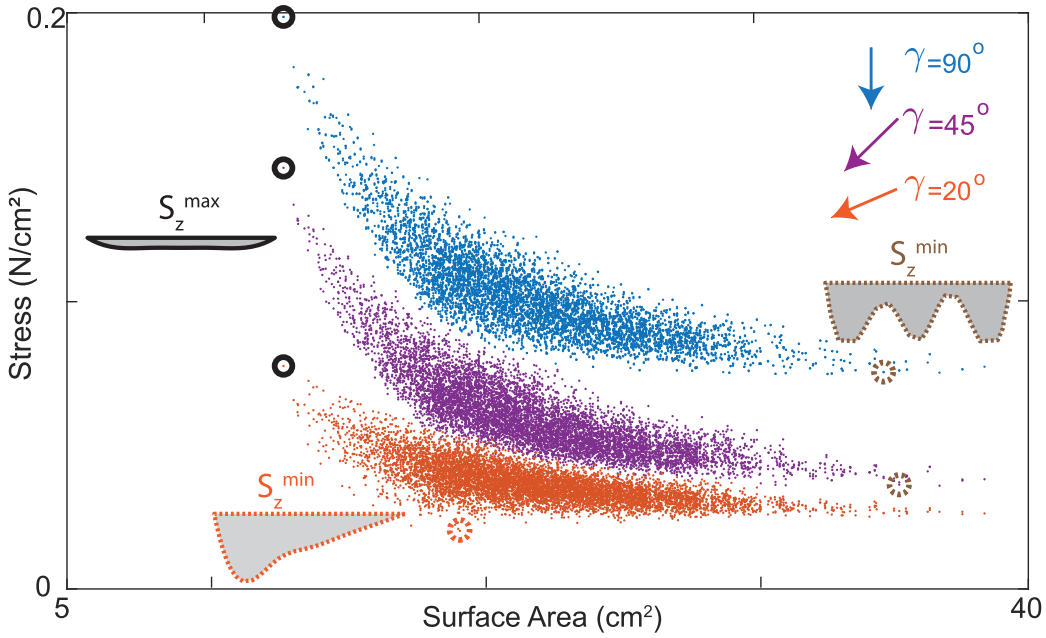

Fig. 9. PRFT peak stress distributions of footpad geometries at an intrusion depth of 5 cm for three different angles of intrusions for $\gamma = [20°,\ 45°,\ 90°]$, shown as orange, purple, and blue dots respectively. (For interpretation of the references to color in this figure legend, the reader is referred to the web version of this article.)

A key factor in footpad design is the mass of the structure. Ideally, the footpad geometry should be lightweight while providing high vertical resistance during landing. This requires evaluating the stress (force per unit area) generated by the footpad geometries, where the unit area can be considered as the unit mass of the footpad. Hence, a footpad geometry that generates higher stress would produce greater force per unit mass. To examine the stress profiles of the footpads, we plotted the stress as a function of their corresponding surface areas, as shown in Fig. 9. The flat surface geometry (shape with a solid black border) produces the highest stresses in all intrusion cases. The smaller surface area of the flat-surfaced footpad contributes to the increased stress. In contrast, the curvy footpad (the shape with a dashed brown border) exhibited the minimal stress for $\gamma = 45°$ and $\gamma = 90°$ due to its larger surface area, while a large wedge-shaped footpad generated the minimal stress at $\gamma = 20°$.

3.4. Testing PRFT predictions of footpad geometries

We validated the accuracy of our PRFT calculations by conducting intrusion experiments using some of the key footpads predicted by our model. We tested three footpad geometries — the wedge-shaped, flat-surfaced, and curvy shape — as illustrated in Fig. 10A–C. Each footpad is penetrated to a depth of 5 cm across three intrusion scenarios ($\gamma = [20°, 45°, 90°]$). The plots in Fig. 10A–C show the force–depth profiles for the tested shapes, with the insets depicting the corresponding stress–depth relationships. The solid curves depict the experimental data for each γ corresponding to the black shapes in the top images, while the dashed curves illustrate the PRFT predictions, which correspond to the red dashed boundary lines in the images.

Our PRFT predictions closely aligned with the experimental results; however, the footpads displayed varying degrees of mismatch under different intrusion conditions. Interestingly, the predictions for wedge shape (Fig. 10A) showed the largest mismatch for $\gamma = 90°$, though PRFT was still able to qualitatively capture the force trend. The predictions for the flat surface (Fig. 10A) were reasonably accurate; however, for $\gamma = 45°$ and $\gamma = 90°$, PRFT failed to capture the bowing trend observed in the force profiles. The forces induced by the curvy footpad (Fig. 10A) are successfully captured by except for $\gamma = 20°$, where underpredicted the forces. This mismatch is thought to arise from the adjacency effects of the wedges (Pravin et al., 2021) and the high variability in the material's volume fraction during intrusion.

Among the shapes tested, the wedge footpad generated the lowest resistive force. The flat surface exhibited increased vertical resistance for all γ, whereas the curvy shape showed the highest resistance for $\gamma = 90°$, exceeding that of the flat surface. In non-vertical intrusions, the curvy shape's resistance was similar to that of the flat surface. Regarding the stress profiles, the flat surface outperformed the others, while the wedge and curvy shapes displayed lower and comparable stress distributions.

The results from our calculations and experiments indicate that if minimizing footpad mass is a priority, a flat surface provides the largest stress distribution across all intrusion scenarios tested. Conversely, if footpad mass is less constrained, a saw-tooth or curved design could be advantageous, as it increases surface area and generates more force, particularly under more vertical intrusion conditions.

4. Conclusion

In this work, drawing on a hypothesis based on frictional plasticity theory and the success of granular RFT (Askari and Kamrin, 2016), we developed a model to predict forces on bodies moving within the dry cohesive powder. This involved calculating the substrate's stress per unit depth by measuring the stresses encountered by a small plate at various attack and intrusion angles and depths. By extending granular RFT, originally developed for non-cohesive media, to include cohesive powder, we verified that the linear superposition of elemental forces acting on an arbitrarily shaped intruder accurately predicts the total forces of the body moving in powder. We demonstrated that powder RFT stress profiles qualitatively align with granular RFT; however, distinct trends emerged between the cohesive and granular stress profiles. Specifically, we observed higher resistance to horizontal intrusions in cohesive powder compared to non-cohesive media. This effect resembled a more isotropic resistance to motion within the powder, which we attributed to the cohesion from interparticle forces in the powder substrate.

Motivated by the needs of NASA JPL's landing missions we tested our model's capabilities by calculating the powder resistive forces on systematically generated geometries. Our goal was to identify geometries that enhance resistance to intrusion in cohesive powder. By

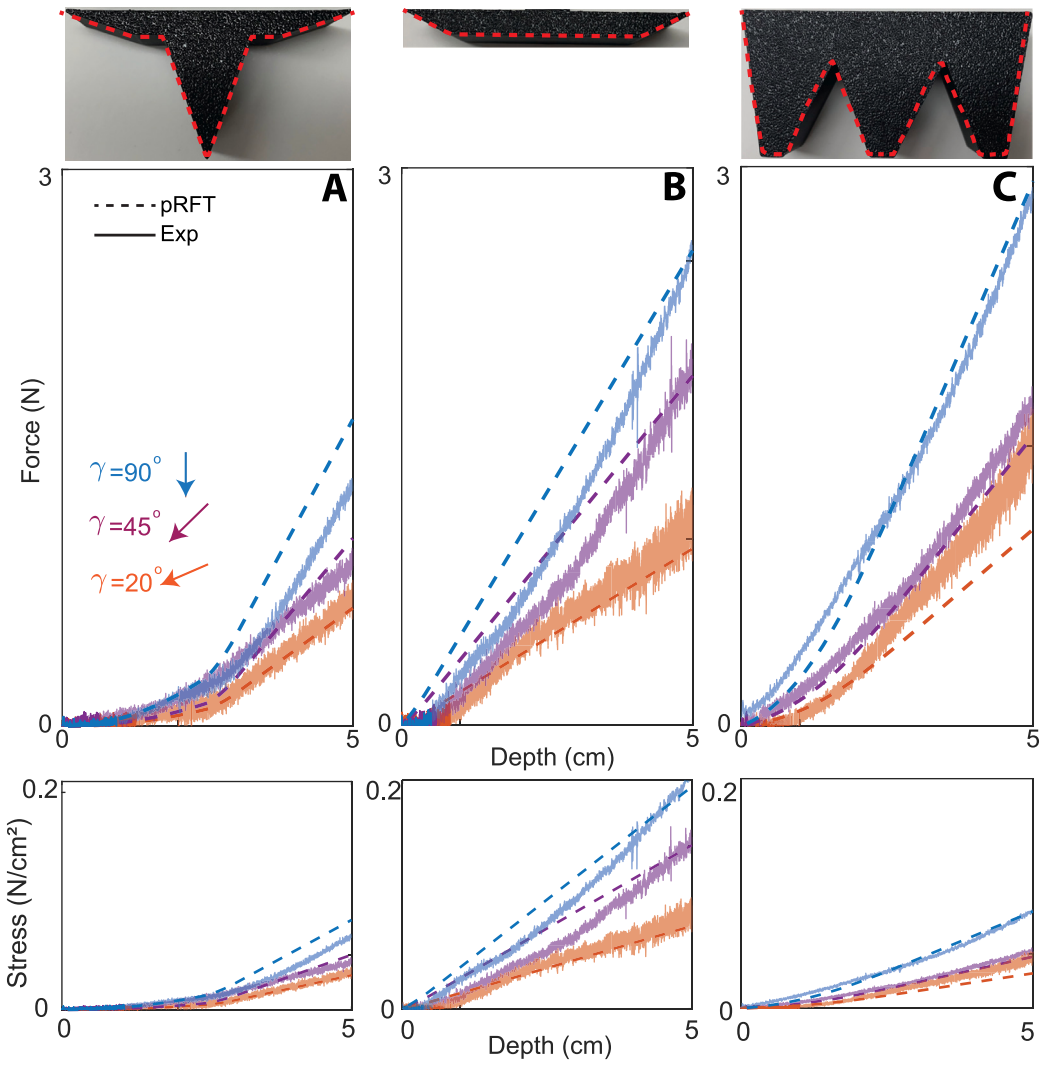

Fig. 10. Force plots of intrusion experiments (solid) versus predictions (dashed) with three intruders under three different angles of intrusion. Insets represent the stress profiles of intruders. Powder intrusions of (A) wedge (B) flat and (C) curvy geometries under near-horizontal (orange), diagonal (purple), and vertical (blue) angles of intrusion. (For interpretation of the references to color in this figure legend, the reader is referred to the web version of this article.)

focusing on planetary lander footpads, we sought to determine which geometries minimize sinkage on weak surfaces, addressing the challenge of landing stability. This is particularly relevant for future missions to Enceladus and Europa, whose surfaces partly consist of loosely consolidated ice powder. Our model's predictions, along with experimental data, indicated that a flat surface provides the highest force distribution per unit footpad mass across a range of intrusion angles. Alternatively, a curvy surface with an increased surface area and mass generated the largest force, particularly under more vertical intrusion conditions. More broadly, we posit that the calculations can be leveraged to design legged and wheeled systems capable of traversing on extremely weak and cohesive terrain.

CRediT authorship contribution statement

Deniz Kerimoglu: Data curation, Formal analysis, Investigation, Methodology, Software, Validation, Visualization, Writing – original draft, Writing – review & editing. **Eloïse Marteau:** Funding acquisition, Methodology, Project administration, Supervision, Writing – original draft, Writing – review & editing. **Daniel Soto:** Investigation, Methodology. **Daniel I. Goldman:** Conceptualization, Formal analysis, Funding acquisition, Investigation, Methodology, Project administration, Supervision, Writing – review & editing.

Declaration of competing interest

The authors declare that they have no known competing financial interests or personal relationships that could have appeared to influence the work reported in this paper.

Acknowledgments

The research was supported by the Strategic University Research Partnerships (SURP) at the Jet Propulsion Laboratory, California Institute of Technology, under a contract with the National Aeronautics and Space Administration, United States (80NM0018D0004). The authors would like to acknowledge Laura Treers for her valuable insights and suggestions and Juntao He for collecting the preliminary data.

References

Agarwal, S., Karsai, A., Goldman, D.I., Kamrin, K., 2021. Surprising simplicity in the modeling of dynamic granular intrusion. Sci. Adv. 7 (17), eabe0631.
Arvidson, R., Bellutta, P., Calef, F., Fraeman, A., Garvin, J.B., Gasnault, O., Grant, J.A., Grotzinger, J., Hamilton, V., Heverly, M., et al., 2014. Terrain physical properties derived from orbital data and the first 360 sols of Mars Science Laboratory Curiosity rover observations in Gale Crater. J. Geophys. Res.: Planets 119 (6), 1322–1344.
Askari, H., Kamrin, K., 2016. Intrusion rheology in grains and other flowable materials. Nat. Mater. 15 (12), 1274–1279.

Bekker, M.G., 1960. Off-the-road locomotion. Res. Dev. Terramechanics.
Bhushan, B., 2009. Biomimetics: lessons from nature–an overview. Philos. Trans. R. Soc. A: Math. Phys. Eng. Sci. 367 (1893), 1445–1486.
Castellanos, A., 2005. The relationship between attractive interparticle forces and bulk behaviour in dry and uncharged fine powders. Adv. Phys. 54 (4), 263–376.
Chong, B., Aydin, Y.O., Gong, C., Sartoretti, G., Wu, Y., Rieser, J.M., Xing, H., Schiebel, P.E., Rankin, J.W., Michel, K.B., et al., 2021. Coordination of lateral body bending and leg movements for sprawled posture quadrupedal locomotion. Int. J. Robot. Res. 40 (4–5), 747–763.
Choukroun, M., Molaro, J.L., Hodyss, R., Marteau, E., Backes, P., Carey, E.M., Dhaouadi, W., Moreland, S., Schulson, E.M., 2020. Strength evolution of ice plume deposit analogs of enceladus and Europa. Geophys. Res. Lett. 47 (15), e2020GL088953.
Dhaouadi, W., Marteau, E., Kolvenbach, H., Choukroun, M., Molaro, J.L., Hodyss, R., Schulson, E.M., 2022. Discrete element modeling of planetary ice analogs: mechanical behavior upon sintering. Granul. Matter 24, 1–20.
Feng, J.Q., Hays, D.A., 2003. Relative importance of electrostatic forces on powder particles. Powder Technol. 135, 65–75.
Fuentes, C., Kang, I., Lee, J., Song, D., Sjöö, M., Choi, J., Lee, S., Nilsson, L., 2019. Fractionation and characterization of starch granules using field-flow fractionation (FFF) and differential scanning calorimetry (DSC). Anal. Bioanal. Chem. 411, 3665–3674.
Golombek, M., Warner, N.H., Grant, J.A., Hauber, E., Ansan, V., Weitz, C.M., Williams, N., Charalambous, C., Wilson, S.A., DeMott, A., et al., 2020. Geology of the InSight landing site on Mars. Nat. Commun. 11 (1), 1014.
Hand, K.P., Phillips, C.B., Murray, A., Garvin, J., Maize, E., Gibbs, R., Reeves, G., San Martin, A., Tan-Wang, G., Krajewski, J., et al., 2022. Science goals and mission architecture of the Europa lander mission concept. Planet. Sci. J. 3 (1), 22.
Harmon, J.M., Cable, M.L., Moreland, S.J., Andrade, J.E., 2023. Predicting the effect of surface properties on enceladus for landing. Planet. Sci. J. 4 (8), 150.
Heiken, G., Vaniman, D., French, B.M., 1991. Lunar Sourcebook: A User's Guide to the Moon. (1259), Cup Archive.
Henann, D.L., Kamrin, K., 2013. A predictive, size-dependent continuum model for dense granular flows. Proc. Natl. Acad. Sci. 110 (17), 6730–6735.
Jabaud, B., Artoni, R., Tobie, G., Le Menn, E., Richard, P., 2024. Cohesive properties of ice powders analogous to fresh plume deposits on Enceladus and Europa. Icarus 409, 115859.
Kamrin, K., 2010. Nonlinear elasto-plastic model for dense granular flow. Int. J. Plast. 26 (2), 167–188.
Kamrin, K., Koval, G., 2012. Nonlocal constitutive relation for steady granular flow. Phys. Rev. Lett. 108 (17), 178301.
Karsai, A., Kerimoglu, D., Soto, D., Ha, S., Zhang, T., Goldman, D.I., 2022. Real-time remodeling of granular terrain for robot locomotion. Adv. Intell. Syst. 4 (12), 2200119.
Lee, J., Hwangbo, J., Wellhausen, L., Koltun, V., Hutter, M., 2020. Learning quadrupedal locomotion over challenging terrain. Sci. Robot. 5 (47), eabc5986.
Li, C., Zhang, T., Goldman, D.I., 2013. A terradynamics of legged locomotion on granular media. Science 339 (6126), 1408–1412.
MacKenzie, S.M., Neveu, M., Davila, A.F., Lunine, J.I., Craft, K.L., Cable, M.L., Phillips-Lander, C.M., Hofgartner, J.D., Eigenbrode, J.L., Waite, J.H., et al., 2021. The Enceladus Orbilander mission concept: Balancing return and resources in the search for life. Planet. Sci. J. 2 (2), 77.
Maladen, R.D., Ding, Y., Li, C., Goldman, D.I., 2009. Undulatory swimming in sand: subsurface locomotion of the sandfish lizard. Science 325 (5938), 314–318.
Maladen, R.D., Ding, Y., Umbanhowar, P.B., Kamor, A., Goldman, D.I., 2011. Mechanical models of sandfish locomotion reveal principles of high performance subsurface sand-swimming. J. R. Soc. Interface 8 (62), 1332–1345.
Marteau, E., Golombek, M., Delage, P., Vrettos, C., Hurst, K.J., Gomez, A., Spohn, T., Ansan, V., Williams, N.R., 2023. Soil mechanical properties at the InSight landing site on Mars. In: AGU Fall Meeting Abstracts, vol. 2023, pp. P44C–04.
Molaro, J.L., Choukroun, M., Phillips, C.B., Phelps, E.S., Hodyss, R., Mitchell, K.L., Lora, J.M., Meirion-Griffith, G., 2019. The microstructural evolution of water ice in the solar system through sintering. J. Geophys. Res.: Planets 124 (2), 243–277.
Moore, H.J., Hutton, R.E., Clow, G., Spitzer, C.R., 1987. Physical Properties of the Surface Materials at the Viking Landing Sites on Mars. Tech. Rep.
Moore, H.J., Jakosky, B.M., 1989. Viking landing sites, remote-sensing observations, and physical properties of Martian surface materials. Icarus 81 (1), 164–184.
Pravin, S., Chang, B., Han, E., London, L., Goldman, D.I., Jaeger, H.M., Hsieh, S.T., 2021. Effect of two parallel intruders on total work during granular penetrations. Phys. Rev. E 104 (2), 024902.
Schofield, A.N., Wroth, P., 1968. Critical State Soil Mechanics, vol. 310, McGraw-hill London.
Shaw, A., Arvidson, R.E., Bonitz, R., Carsten, J., Keller, H., Lemmon, M.T., Mellon, M.T., Robinson, M., Trebi-Ollennu, A., 2009. Phoenix soil physical properties investigation. J. Geophys. Res.: Planets 114 (E1).
Skonieczny, K., Niksirat, P., Nassiraei, A.A.F., 2019. Rapid automated soil preparation for testing planetary rover-soil interactions aboard reduced-gravity aircraft. J. Terramechanics 83, 35–44.
Slyuta, E., 2014. Physical and mechanical properties of the lunar soil (a review). Sol. Syst. Res. 48, 330–353.
Suzuki, H., Katsushima, K., Ozaki, S., 2019. Study on applicability of RFT to traveling analysis of wheel with grousers: Comparison with DEM analysis as a virtual test. J. Terramechanics 83, 15–24.
Team, R., 1997. Characterization of the Martian surface deposits by the Mars Pathfinder rover, Sojourner. Science 278 (5344), 1765–1768.
Treers, L.K., McInroe, B., Full, R.J., Stuart, H.S., 2022. Mole crab-inspired vertical self-burrowing. Front. Robot. AI 9, 999392.
Vaquero, T.S., Daddi, G., Thakker, R., Paton, M., Jasour, A., Strub, M.P., Swan, R.M., Royce, R., Gildner, M., Tosi, P., et al., 2024. EELS: Autonomous snake-like robot with task and motion planning capabilities for ice world exploration. Sci. Robot. 9 (88), eadh8332.
Winters, H., 1968. Lunar module/lm/soil mechanics study, volume 1 final report, may 1966-feb. 1968. Tech. Rep.